23

Radiation Dynamics from the Ultra-Intense Field Ionization of Atoms

Isaac Ghebregziabher and Barry Walker
University Of Delaware
USA

1. Introduction

The interaction of high-intensity and ultrashort lasers with matter produces high energy particles and photons. Recent experiments include the generation of high quality GeV electron (Kneip et al., 2009; Leemans et al., 2006) and multi-MeV proton (Clark et al., 2000; Snavely et al., 2000) beams in laser plasma interactions. Different schemes can now be followed to produce ultra-short x-ray radiation. The production of keV x-rays from betatron oscillations of relativistic electrons in plasma channels was demonstrated 5 years ago (Rousse et al., 2004). Femtosecond x-ray beams have also been detected when high energy laser pulses cross relativistic electrons from a conventional linear electron accelerator (LINAC) (Schoenlein et al., 1996). Recently, an ultrashort x-ray pulse has been produced from the scattering of an ultrashort laser pulse off a laser generated relativistic electron beam (Schwoerer et al., 2006). The primary processes of x-ray generation are the ionization of an atom/ion and the subsequent acceleration of photoelectrons to relativistic energies in the intense laser field. A detailed description of radiation from laser-atom interaction is necessary to fully understand the mechanism behind x-ray generation from laser-plasma interactions and there is a growing interest in the physics of the radiation from laser acceleration of photoionization at relativistic intensities (Chowdhury et al., 2005).

In this chapter we focus on the generation of x-ray photons by Thomson scattering from atomic ionization in ultra-strong laser fields. When an atom is submitted to an ultra-strong laser field, the laser electric field $\mathbf{E}_{laser}$ suppresses the Coulomb barrier and the outermost electron ionizes as it tunnels through the suppressed barrier. Photoelectrons ionized in an ultra-strong field $1 \times 10^{18}\ W/cm^2$ are accelerated to a relativistic speed in a fraction of an optical cycle, the magnetic field of the ionizing laser field becomes significant and the motion of these ionized free electrons is nonlinear. Through its relativistic and non-linear motion, the electron may emit radiation at high harmonics of the drive field frequency in a process known as non-linear Thomson scattering.

During tunneling ionization, the ultra-strong laser field leaks out an electron wave packet out of an atom at a finite rate, typically every half cycle of the laser field. For each ionization event, the electron wave packet spreads to a spatial dimension from nm to μm over the interaction time of the laser field. The electron may also radiate as it is relativistically accelerated in the ultra-strong laser field. It becomes natural to ask how this spatially extended relativistically driven electron wave packet may radiate. Different parts of the

Source: Advances in Solid-State Lasers: Development and Applications, Book edited by: Mikhail Grishin,
ISBN 978-953-7619-80-0, pp. 630, February 2010, INTECH, Croatia, downloaded from SCIYO.COM

electron wave function experience different phases of the laser field and the emitted radiation from each segment of the ionization current could interfere constructively/ destructively to enhance/suppress the emitted radiation in the far field. In sections 3 and 4 results and discussion will be presented on the effects of electron wave-function spreading and interference on radiation from atomic ionization in ultrastrong laser fields. We compare emitted radiation calculated with a classical electron (point charge) and semi-classical model which allows interference. We wish to clarify the impact of an incoherent versus a coherent treatment of the radiation from photoelectrons when the ionization, i.e., tunneling, is coherently driven. Though there are some indications from plasma experiments the process may be incoherent (Chen et al., 1998; Phuoc et al., 2003), it is not known experimentally whether radiation from coherently ionized and field accelerated photoelectrons in ultrastrong fields is incoherent, coherent, or partially coherent. The results are presented here for 800 nm laser radiation, but similar results are expected for other visible and IR laser wavelengths (Ueshima et al., 1999; Tate et al., 2007).

In the semi-classical model, for each ionization event, the ionization probability is multiplied by an electron charge to approximate the extended electron wave function in the continuum. This approximate model of the quantum electron doesn't allow us to investigate the effect of phase of the electronic wave function on the emitted radiation. An exact quantum mechanical treatment of the problem is required to investigate phase effects on radiation. However, to a good approximation the effects of electron wave packet spreading and interference from an extended charge distribution could well be captured with in our semi-classical model since the quantum mechanical charge distribution is usually represented by the modulus squared of the electron wave-function which erases any phase information associated with the electron wave-function.

Previous works (Mocken & Keitel, 2005) have shown deviations in the emitted radiation spectrum from a classical and an arbitrary prepared electron wave packet in a plane wave laser field. Recently, one paper (Peatross et al., 2008) has considered emitted radiation from a single electron wave packet by establishing a relation between the exact quantum formulation and its classical counterpart via the electron's Wigner function and has asserted that the electron radiates like a point like emitter. Both of these works ignore ionization and calculate the emitted radiation from a free electron interacting with an intense laser field. Future experiments on radiation from atomic ionization would shed light on how a photoelectron radiates and would vaildate/invalidate our semi-classical approach to the calculation of the radiation (Ghebregziabher & Walker, 2008).

1.1 Exact treatment of ultra-strong laser fields

Another fundamental question arises on how to describe the ultrastrong laser field when calculating the emitted radiation from photoelectrons accelerated in ultrastrong laser focus. To achieve high intensities the laser field is usually focused to a miniature focal spot, typically several μm in size at full width half maximum (FWHM). In strong field physics, electron excursion extends out to nm length scale and the plane wave approximation to the laser field is valid. Because in strong fields $\beta \approx 0$, electron dynamics is mainly affected by the electric field component of the laser field. The magnetic field component of the laser may be neglected and photoelectron dynamics is easily obtained by solving non-relativistic equation motion.

In ultra-strong laser fields photoelectron dynamics is relativistic ($\beta \neq 0$) and non-linear. With in a plane wave approximation to the laser field an analytic solution to the relativistic

photoelectron dynamics is readily available (Lau et al., 2003). Figure 1 shows the co-ordinates of an electron born with zero initial speed at $t_{in} = 0$ and $z_{in} = 0$ in a plane wave laser field with an $800nm$ central wavelength and field strengths $a = 0.5$, $a = 1.53$, and $a = 3$ corresponding to laser intensities of $5 \times 10^{17}\ W/cm^2$, $5 \times 10^{18}\ W/cm^2$, and $2 \times 10^{19}\ W/cm^2$, respectively. The coordinates are shown for 3 optical cycles. The figure shows for laser intensities where the field strength parameter $a > 1$, the width of the photoelectron drift along the propagation direction (z-axis) is greater than the quiver width along the polarization axis (x-axis). Moreover, electron quiver width for $a > 1$ is greater than 0.3 μm. specifically, for a field strength $a = 3$, the quiver width is 0.8 μm. Realistic laser focus has a finite spatial extent. Typically, in ultrastrong fields, the full width at half maximum (FWHM) beam diameter could be 2 to 3 microns, which is only a factor of 2 times the electron excursion width in an optical cycle. In reality the laser focus has curved wave fronts that depend on space. Therefore, adopting plane wave approximation in an ultrastrong laser field is not valid.

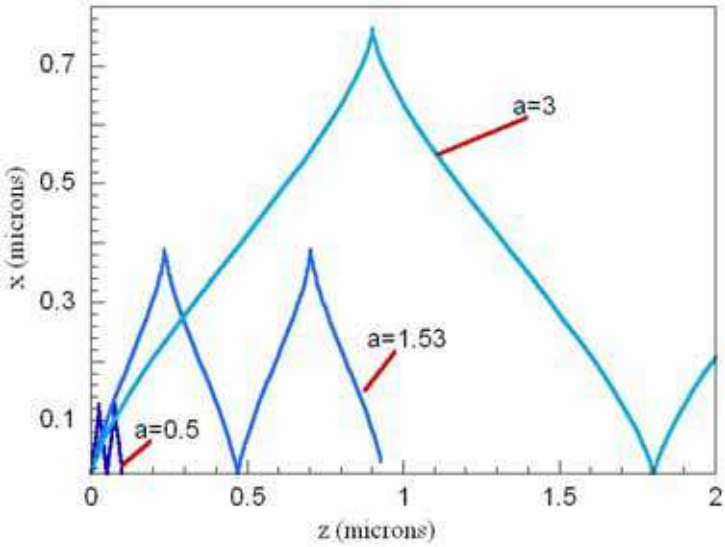

Fig. 1. Parametric plot of x versus z coordinates for an electron ionized at t=0 and z=0 for three different laser intensities corresponding to field strength of 0.5, 1.53, and 3.

To a leading order the paraxial approximation to the laser field may be adopted to solve the dynamics more accurately. In the paraxial approximation, the longitudinal field components are neglected, i.e., for a laser field polarized along the x-axis and propagating along the z-axis, the non-zero field components are E_x and B_y. These transverse field components confine the electron dynamics in the x-z plane. Such an approximation may be valid when describing photoelectron dynamics inside a laser focus with electron excursion much smaller than the waist diameter of the laser focus. However, to achieve ultrastrong laser fields, the laser field is focused to a small spot size. For instance, the diffraction limited focal spot size of a laser field with 800 nm central wavelength when focused with an f/# 1.5 parabolic mirror is about $2.42\mu m$. In such a tight laser focus consistency with Maxwell's equations requires non-zero longitudinal fields. Previous works, see for example (Barton &

Alexander, 1989; Davis, 1979) have shown that the laser field could be described to any desired accuracy as a series expansion of the diffraction parameter $\epsilon = \lambda/(2\pi s_0)$, where λ is the carrier wave length and s_0 is waist diameter of the beam at $\exp^{-2}$. Here we give the field components accurate on the order of ϵ^3 for a laser field polarized along the x-axis and propagating in the z-axis.

$$\begin{aligned}
E_x &= \tilde{E}\left[\cos(\Phi+\alpha)+\varepsilon^2\left\{\frac{2x^2+r^2}{s(z)^2}\cos(\Phi+3\alpha)-\frac{r^4}{s(z)^3 s_0}\cos(\Phi+4\alpha)\right\}\right] \\
E_y &= \varepsilon^2\tilde{E}\frac{2xy}{s(z)^2}\cos(\Phi+3\alpha) \\
E_z &= -2\tilde{E}\varepsilon\frac{x}{s(z)}\left[\sin(\Phi+2\alpha)+\varepsilon^2\frac{r^2}{s(z)^2}\left\{3\sin(\Phi+4\alpha)-\frac{r^2}{s(z)s_0}\cos(\Phi+5\alpha)\right\}\right] \\
B_x &= E_y \\
B_y &= \tilde{E}\left[\cos(\Phi+\alpha)+\varepsilon^2\left\{\frac{2y^2+r^2}{s(z)^2}\cos(\Phi+3\alpha)-\frac{r^4}{s(z)^3 s_0}\cos(\Phi+4\alpha)\right\}\right] \\
B_z &= E_z\frac{y}{x},
\end{aligned} \tag{1}$$

where,

$$\begin{aligned}
\tilde{E} &= E_0\frac{s_0}{s(z)}\exp\left(-\frac{r^2}{s(z)^2}\right) \\
r^2 &= x^2+y^2 \\
\Phi &= \omega_0 t - kz - \frac{zr^2}{z_R s(z)^2} \\
\alpha &= \arctan\left(\frac{z}{z_R}\right), z_R = \frac{ks_0^2}{2}.
\end{aligned}$$

Where E_0 is the laser field amplitude, z_R is the rayleigh length and $s(z)$ is the beam diameter at a given propagation distance. Figure 2 (a) shows contour plot of the spatial profile of the nonparaxial laser field E_z and the largest electric field component E_x (b). The longitudinal field component E_z is a factor of 6 less than the transverse field component E_x, see Fig. 2. The figure also shows that longitudinal field components are not only non-zero but also exhibit different spatial profile compared to the transverse field components. This is evident from figure 2 where the field component E_z is asymmetric with respect to reflection about the origin while E_x preserves symmetry with reflection. Moreover, E_z vanishes on axis, i.e., $E_z = 0$ for $x = 0$ while E_x has the largest amplitude.

These complicated field structures expose photoelectrons to rather complicated dynamics. In section 5 of this chapter we compare the traditional plane wave approximation treatment of the laser field with our new results that include the 3-dimensional nature of the focused laser field with curved wave fronts to provide framework for experimental events, i.e., when should observations be compared to the plane wave results and what is the primary impact of the focus geometry used in experiments. This treatment includes the fact that electrons ionized at the same axial position but different radial positions will be accelerated by different phases of

the laser field. The results presented here extend previous works of an electron interacting with an intense electromagnetic field (Lee et al., 2005; Esarey et al., 1993; Keitel & Knight, 1995; Hu & Starace, 2002) by including the ionization process itself as it affects the phase of the driving field for the photoelectrons and coherence properties of the emitted radiation.

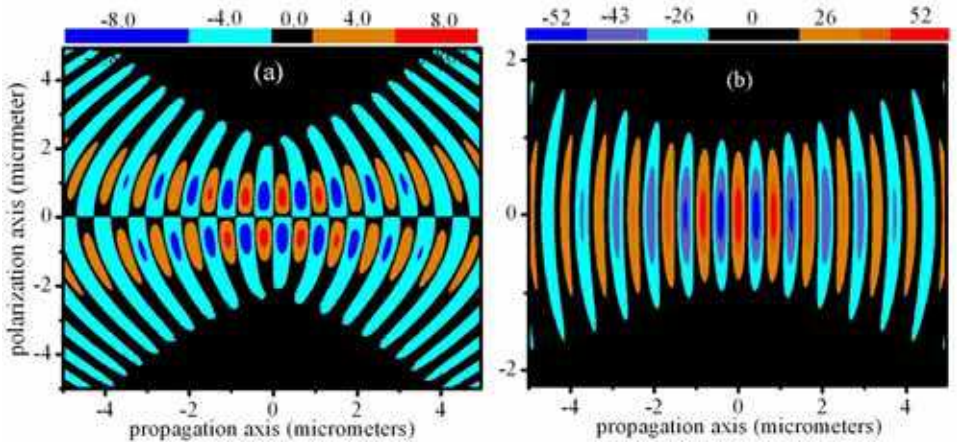

Fig. 2. Contour plot of the spatial profile of E_z (x, y = 0, z) (a) and E_x (x y = 0, z) (b) (with field strengths given in atomic units). The laser beam waist diameter is 1.52 μm and the peak laser intensity is $1 \times 10^{20}\, W/cm^2$.

2. The radiation model

Every aspect of the radiation would be appropriately predicted if one solves the Dirac equation in 3+1 dimensions given by

$$i\hbar \frac{\partial \psi}{\partial t} = c\vec{\alpha} \cdot \left(\frac{\hbar}{i} \vec{\nabla} - \frac{q}{c} \vec{A} \right) \psi + (V(r) + \beta mc^2)\psi \tag{2}$$

where $\vec{A}$ is the laser field vector potential, q is the charge of an electron, m is the rest mass of an electron, c is the speed of light, $V(r)$ the Coulomb potential and α^i and β are the usual Dirac matrices (i = 1, 2, 3). It requires large spatial grid sizes with exteremely small time steps to solve eqn. 2 numerically. One paper (Mocken & Keitel, 2005) based on Dirac charge current and classical electrodynamics outlines a procedure to calculate the radiation spectrum emitted by an arbitrarily prepared Dirac wave packet and has shown deviations to the purely classical calculations in the high frequency part of the radiated spectrum. To the best of our knowledge there exists no fully quantum mechanical calculation of radiated field from atomic ionization that takes into account ionization dynamics and the 3-dimensional nature of the ionizing ultrastrong laser field. We circumvent this problem by employing a semiclassical trajectory ensemble model to represent the electron wavefunction in the continuum, which has been successful in predicting correlated multielectron ionization (Palaniyappan et al., 2006) and the cutoff photon energy associated with higher-order harmonic generation (Corkum, 1993). With the simplified semiclassical trajectory ensemble representation of the electron wave function, we developed a four step ultrastrong radiation model divided as follows:

1. Atomic photoionization
2. Relativistic dynamics for the electron
3. Calculation of radiation from relativistic electrons
4. Superposition of the radiation across the laser focus

2.1 Classical and semiclassical ionization dynamics

In the first part of the radiation model, atomic photoionization, classical and semiclassical ionization models are considered. For classical ionization, the strong field tunneling ionization is merged with a Monte Carlo (MC) technique which has been described in (Ghebregziabher & Walker, 2007). In the classical model, the ionization rate during the laser pulse is first calculated according to the the ionization based on hydrogen orbitals extended to complex atoms by Ammosov, Delone, and Krainov (ADK) (Ammosov et al., 1986) (ADK) tunneling ionization model for each phase of the laser field. The ADK theory is essentially an extension of Perelomov, Popov, and Terentev (PPT) (Perelomov et al., 1966) theory where states of complex atoms are characterized by effective principal and orbital quantum numbers. The ionization rate is then normalized to the peak rate at the center of the focus, peak of the pulse. If the normalized rate exceeds 10^{-3} a comparison is made with a randomly generated number between zero and one. When the normalized ionization rate is greater than the randomly generated number, ionization is allowed 50% of the time (again determined by chance) and a single classical electron is liberated to the continuum from its bound state. Over many events this assignment of ionization provides a linear mapping of rate to ionization events. The tunneling ionization treatment used in this paper limits the maximum intensity to approximately $1 \times 10^{20}\ W/cm^2$, beyond this intensity the laser magnetic field and relativistic effects may affect the fundamental ionization mechanism (Popov, 2004). No experimental measurements have verified the atomic ionization mechanism above a few times $1 \times 10^{20}\ W/cm^2$.

For semiclassical calculations, ionization for a single atom is calculated according to ADK tunneling for each phase of the laser pulse. Rather than a discrete ionization event as in the MC ADK case, here a trajectory ensemble weighted by the fractional ionization probability for that phase is liberated to the continuum. In this semiclassical ionization model, the trajectory ensemble weighted by the ionization probability is an approximation for the tunneling probability current of the quantum electron. In Fig. 3(a) the appearance of the electron probability in the continuum is plotted as a function of time and shown to be very similar for the classical MC ADK and semiclassical ADK calculation. It is important to note the MC ADK classical ionization case (which for a single event is a step function) is shown for many MC events and so represents an average. In Fig. 3(b,c) the spatial distribution of the electron probability after a single atom interacts with the field for few cycles is shown. While classical ionization gives rise to a single point electron (b) the tunneling ionization current appears continuously (c) with maximum bursts at the peaks of the electric field.

The ionization contribution is generally considered from a single charge state; Ne^{8+} at $2\times10^{17}\ W/cm^2$, Ar^{10+} at $2 \times 10^{18}\ W/cm^2$, Ar^{16+} at $1.2 \times 10^{19}\ W/cm^2$, Na^{10+} at $5 \times 10^{19}\ W/cm^2$, and Na^{11+} at $1.2 \times 10^{20}\ W/cm^2$. Results for ionization from multiple charge states preceding the peak intensity have also been calculated and will be presented in the final sections of the chapter. These ions were chosen because they have a net ionization probability at the specified intensity of typically 10^{-3} to 10^{-2}. A cluster of 32 Opterons with 2.4 GHz processors were used for these calculations.

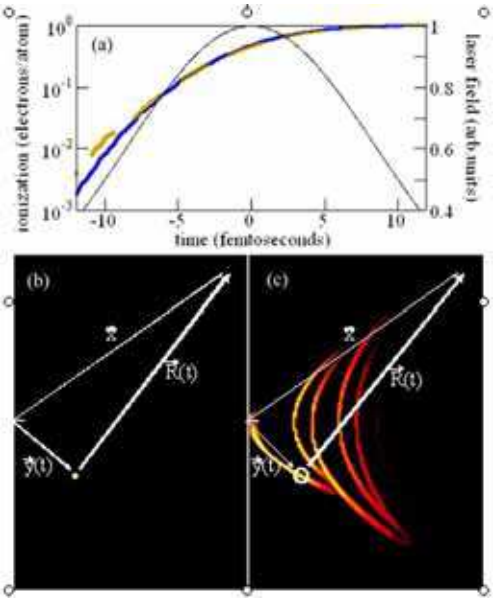

Fig. 3. Plot of ionization probability (a) as a function of time across the laser pulse (thin line) for the MC-tunneling (dashed) classical model and tunneling ionization probability current (wide line) semiclassical tunneling. Shown in (b,c) are 2D plots of the electron density for a classical electron (dot, b) and the tunneling ionization probability current (c) in a 75nm (horizontal, k) by 800nm (vertical, E) frame from an atom ionizing (located at the white tick on the left-center of each frame) a few cycles after ionization begins. Superimposed on the frames are the vector x, y, and R for the case when the atom is located at the origin. In (c) a representative charge segment $f_j q$ is circled in white.

2.2 Photoelectron continuum dynamics

For both classical and semi-classical ionization methods, the photoelectron dynamics are calculated by solving the relativistic equations of motion given as:

$$\begin{aligned}
\frac{dp_x}{dt} &= q\left(E_x + \frac{p_y}{\gamma m_0 c}B_z - \frac{p_z}{\gamma m_0 c}B_y\right) \\
\frac{dp_y}{dt} &= q\left(E_y + \frac{p_z}{\gamma m_0 c}B_x - \frac{p_x}{\gamma m_0 c}B_z\right) \\
\frac{dp_z}{dt} &= q\left(E_z + \frac{p_x}{\gamma m_0 c}B_y - \frac{p_y}{\gamma m_0 c}B_x\right) \\
\frac{dx}{dt} &= \frac{p_x}{m\gamma} \\
\frac{dy}{dt} &= \frac{p_y}{m\gamma} \\
\frac{dz}{dt} &= \frac{p_z}{m\gamma}
\end{aligned} \tag{3}$$

Where m_0 is the rest mass of an electron, q the charge of an ensemble member, $\mathbf{p}$ the particles momentum, $\mathbf{E}$ and $\mathbf{B}$ are the laser magnetic and electric field vectors, and γ is the well known relativistic lorentz factor. Implicit in the notation of the laser electric and magnetic fields is the time and space dependence of the fields, for example $E_x = E_x(\mathbf{r}, t)$. Notice that non-paraxial field components are included in equation 3.

We use a Runge-Kutta ordinary differential equation solver with relative error tolerance threshold of 10^{-6}, local error threshold of 10^{-12}, and time step typically of the order $10^{-4} fs$ to solve photoelectron dynamics (Eqn. 3). The laser pulse used for these calculations ($\mathbf{E}_{laser}$, $\mathbf{B}_{laser}$ linear polarization, 800 nm central wavelength, and 20 fs full width at half maximum Gaussian temporal profile) is comparable to current high field experiments (Albert et al., 2000). Two different spatial modes are considered: a plane wave and a f/# 1.5 TEM_{00} nonparaxial laser focus calculated to a field accuracy of 0.5%, i.e., third order non-paraxial terms. Fifth order non-paraxial field terms have also been included but the resulting dynamics didn't change from the dynamics calculated with third order accuracy. Since the scattered radiation comes from relativistic photoelectron dynamics in the laser focus, the accuracy of the calculated radiation yield will be limited by how much photoelectron dynamics is impacted when approximating the laser field with paraxial solution.

Since the motion is on the scale of nm to μm and the electron energies are of order 10 times the ionization potential energy, the Coulomb field of the core atom or ion does not affect the dynamics. Also the interaction is considered in the low-density limit so space charge effects and hard collisions (collisions with low impact parameters) are neglected. Radiation damping is not accounted for in the calculation since the ratio of the total radiated energy per cycle to the average kinetic energy of the electron is less than 10^{-6}.

In the limit of low fields ($< 1 \times 10^{16}\ W/cm^2$) or weakly focused geometries, the paraxial approximation to the laser field is valid and simplifications occur in the relativistic equations of motion given by Eqn. 3. In this case, a relativistically invariant relationship between the longitudinal and transverse momenta of the photoelectron at the end of the laser pulse exists, i.e., $p_z = p_x^2/2mc$ or equivalently $\tan(\theta) = \sqrt{2/(\gamma - 1)}$ where θ is the polar angle from the propagation axis (z). Figure 4 is a snapshot of the electron probability projected on the x-z plane from ionization of Ar^{8+} at the peak of the pulse with an intensity of $2 \times 10^{18}\ W/cm^2$ and Ar^{15+} at an intensity of $1 \times 10^{19}\ W/cm^2$. As one can see from figure 4(a) photoelectron dynamics is relativistic at an intensity of $2 \times 10^{18}\ W/cm^2$ as shown by drift along z. However, as the extent of the probability distribution is near the center of the focus the continuum may be approximately described by $p_z = p_x^2/2mc$ dynamics with a spatially uniform electric and magnetic field. For the electric charge distributions in Fig. 4(a), $\mathbf{k} \cdot \mathbf{r}$ is less than 1 and γ is less than 1.1. With these conditions the electron will oscillate in phase with the laser field and the parabolic relationship between p_x and p_z will result in a similar relationship between the x and z components of the drift velocity causing the wave fronts to become parabolic.

Photoelectron dynamics for the higher laser intensity ($1 \times 10^{19}\ W/cm^2$) is clearly different, as can be seen from Fig. 4(b), with the electron probability from each tunneling ionization "burst" distributed over a $10^{-6} m$ length scale, which is comparable to the focus and wavelength dimension. Although near the center of the f/# 1.5 TEM_{00} mode laser focus the field is nearly paraxial, the large electron velocity at $1 \times 10^{19} W/cm^2$ $\gamma \simeq 2$ destroys the parabolic relationship between the x and z components of the drift velocities. As shown in

Fig. 4(b), a significant amount of electron probability approaches the Raleigh length while the field is still large, a scenario made possible by large $\mathbf{k} \cdot \mathbf{r}$, the motion is dominated by non-paraxial fields, which are very different from the paraxial fields in phase and amplitude.

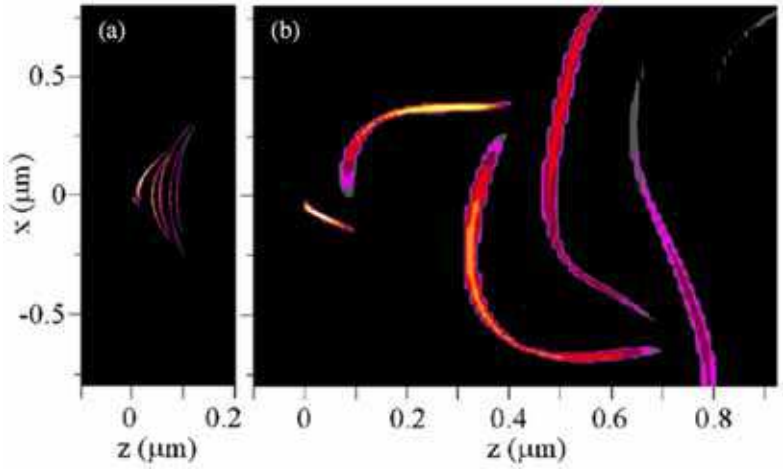

Fig. 4. Semiclassical ensemble trajectory electron probability from atomic ionization at $2 \times 10^{18} W/cm^2$ (a), and $1 \times 10^{19} W/cm^2$ (b). The electron probability is shown in a normalized log color scale with one color per factor exp(-1).

2.3 Radiation from relativistic charges

Once the dynamics is solved with the above equations, the radiated energy from a relativistic charge could be obtained with Lienard-Wiechert potential (Jackson, 1975). The radiated electric field is obtained with the equation given by:

$$\vec{E}(\vec{R},t) = \frac{q}{4\pi c}\left(\frac{\hat{n} \times ((\hat{n} - \vec{\beta}) \times \dot{\vec{\beta}})}{(1 - \hat{n} \cdot \vec{\beta})|\vec{R}|}\right). \tag{4}$$

where $R(t) = |\vec{x} - \vec{y}(t)|, \hat{n} = \frac{\vec{x} - \vec{y}(t)}{R(t)}, \vec{\beta(t)} = \frac{\vec{y(t)}}{c} = \frac{1}{c}\frac{dy}{dt}(t)$ and c is the speed of light. Since $|\vec{x}| \gg |\vec{y}|, R^2 \cong |\vec{x}|^2$. For the purposes of comparison, all reported fields and radiated energies are normalized for a yield expected from a single electron. The vectors $\vec{x}, \vec{y}$, and $\vec{R(t)}$ are shown superimposed on Fig. 3 (b,c). With the temporal and spatial intensity changes in a laser focus there are corresponding changes in the photoelectron velocity and acceleration. From eqn. 4 it is easy to see that the intensity of the radiated photons from a relativistically moving charge is proportional to the following parameter:

$$f = \frac{\hat{n} \times \left[\left(\hat{n} \times \vec{\beta}\right) \times \dot{\vec{\beta}}\right]}{\left(1 - \hat{n} \cdot \vec{\beta}\right)^3} = \frac{\hat{n} \cdot \dot{\vec{\beta}}(\hat{n} - \vec{\beta}) - \dot{\vec{\beta}}(1 - \hat{n} \cdot \dot{\vec{\beta}})}{\left(1 - \hat{n} \cdot \vec{\beta}\right)^3} \tag{5}$$

where $R(t) = |\vec{x} - \vec{y}(t)|, \hat{n} = \frac{\vec{x} - \vec{y}(t)}{R(t)}, \vec{\beta(t)} = \frac{\vec{y(t)}}{c} = \frac{1}{c}\frac{dy}{dt}(t)$ and c is the speed of light. In the limit where v/c approaches unity, the parameter f given in eqn. 5 is largest for electron velocities aligned with the detector at $\vec{x}$, i.e. $\vec{\beta} \cong \hat{n}$, and accelerations perpendicular to the line of sight to the detector i.e., $\hat{n} \cdot \dot{\vec{\beta}} = 0$. For these instances, $(\vec{\beta} \cong \hat{n}, \hat{n} \cdot \dot{\vec{\beta}} = 0)$ the parameter given in eqn. 5 simplifies to the form.

$$\lim_{v/c \to 1} = \frac{\dot{\vec{\beta}}}{\left(1 - \hat{n} \cdot \vec{\beta}\right)^2} \tag{6}$$

The parameter f is used here to provide insight into the dynamics and show which regions of the laser focus are responsible for the highest radiation yields. This parameter calculated for 5000 electron trajectories is shown in Fig. 5 for laser intensities of $2 \times 10^{17}\ W/cm^2$, $2 \times 10^{18}\ W/cm^2$ and $1.2 \times 10^{19}\ W/cm^2$. At an intensity of $2 \times 10^{17}\ W/cm^2$ (Fig. 5(a)) the electron motion is largely non-relativistic with a peak $\gamma = \left(\sqrt{1 - \frac{v^2}{c^2}}\right)^{-1}$ = 1.05 and the denominator of equation (6) may be neglected. The motion associated with radiation via the parameter f has a distribution that mimics the ionization distribution and spatial intensity profile of the laser focus. The radiation in this case comes from the center of the focus where the photoelectron experiences the highest intensity.

At an intensity of $2{\times}10^{18}\ W/cm^2$ (Fig. 5b) relativistic effects with a peak $\gamma = \left(\sqrt{1 - \frac{v^2}{c^2}}\right)^{-1}$ = 1.5 start to kick in and the motion associated with radiation via the parameter f has a distribution that extends beyond the peak region of highest intensity.

As the intensity is increased to $1.22{\times}10^{20}\ W/cm^2$ (see Fig. 5(c)), the electron motion is highly relativistic and the dynamics change with an electron excursion comparable to the size of the laser focus. As the electron leaves the focus, the laser imparts an extra boost of speed in a process known as „surfing" coined from the wave like „winged" pattern for f in Fig. 5(c). Counter intuitively, the regions of the highest laser intensities near the center of the focus do not result in the best conditions for radiation. Rather, at ultrahigh intensities and focused geometries the radiation may be expected to come when the photoelectron is off the peak of the laser focus.

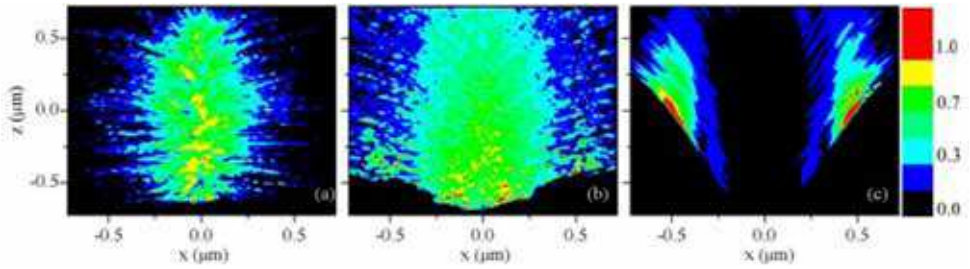

Fig. 5. Contour plot of the parameter f for laser intensities of $2 \times 10^{17}\ W/cm^2$(a), $2 \times 10^{18}\ W/cm^2$(b) and $1.22 \times 10^{20}\ W/cm^2$ (c). The magnitude scale for f is linear and normalized in each case.

2.4 Superposition of the radiation

With the emitted field obtained with Eqn. 4, the total radiated electric field is calculated by summing coherently and incoherently across the ionization current and laser focus in the focused geometry case. In the plane wave (1D) classical ionization case the yield we report in this chapter represents an average of hundreds to thousands of Monte Carlo photoelectrons for atomic ionization across a broad range of phases. Most of the radiation comes from electrons ionized at the peak of the field, however, the method accurately accounts for „off peak" ionization rates. For a single MC-ADK ionization event, the emitted electric field is given by Eq. 4. For a number of atoms ionized N, the total radiated energy is the classical total radiated energy, W_C, per unit solid angle normalized to an average yield per photoelectron given by:

$$\frac{dW_c}{d\Omega} = \left(\frac{c}{4\pi}\right)\frac{R^2}{N}\sum_{i=1}^{N}\int_{-\infty}^{\infty}\left|\vec{E}(\vec{R},t)\right|^2 dt \tag{7}$$

In the plane wave, semi-classical treatment a single atom is adequate to accurately capture the emitted field response from the ionization current since ionization occurs over all phases; however, the normalization for the fractional ionization must be correctly taken into account. For a total number of M phase steps that comprise the semi-classical ensemble, the radiated electric field from the j^{th} phase step of the ensemble $\vec{E}_j(\vec{R},t)$ is obtained by replacing q in Eq. 4 with the weighted charge $f_j q$, where f_j is the fractional ionization probability at a given laser phase (see Fig. 3(c)). For incoherent and coherent superposition of the radiation from the tunneling probability current, the sum of the radiation and normalization must be done differently. For the incoherent case, the total radiated energy per unit solid angle from the SC tunneling probability ionization current is given by:

$$\frac{dW_{sc-incoherent}}{d\Omega} = \left(\frac{c}{4\pi}\right)R^2\int_{-\infty}^{\infty}\left\{\frac{\sum_j^M\left(\vec{E}(\vec{R},t)\right)^2}{\sum_j^M f_j^2(t)}\right\}dt \tag{8}$$

In the case of a coherent superposition of the radiation from the tunneling probability current, $\vec{E}_j(\vec{R},t)$ must be summed before being squared to allow for interference, i.e., $\vec{E}_{sc-coherent}(\vec{R},t)=\sum_{i=1}^{M}\vec{E}_j(\vec{R},t)$. The total radiated power per single electron ionization event is then calculated by normalizing to the total ionization probability squared,

$$\frac{dW_{sc-coherent}}{d\Omega} = \left(\frac{c}{4\pi}\right)R^2\int_{-\infty}^{\infty}\left\{\frac{\left(\sum_j^M\vec{E}(\vec{R},t)\right)^2}{\left(\sum_j^M f_j(t)\right)^2}\right\}dt \tag{9}$$

Here again M is the sum over the SC ensemble, not the sum over the ionization from different atoms.

The previous cases (Eq. 8- 9) address the radiation from the interaction of the atom with a plane wave. Calculations for atoms distributed in a three dimensional laser focus (3D) include an addition spatial sum for the radiation across all the ionizing atoms in the focus. Spatial summations for radiation between different atoms in all cases (i.e. W_C, $W_{SC-incoherent}$, $W_{SC-coherent}$) are done coherently; the total radiation field is equal to the sum of the fields from

all the atoms. For the classical case, the form of Eq. 7 is the same but the index N represents a sum of all ionization events across the focus and not an average of many atoms at a single location as for the plane wave case. In the SC tunneling probability current case, an additional sum is included over the N atoms ionizing in the laser focus incorporated as shown in Eqs. 10 and 11. It is important to note that $W_{SC-incoherent}$ in the focal geometry case involves an incoherent sum of the radiation from the tunneling ionization probability for a single atom but a coherent sum of the radiation between different atoms. For the fully coherent case $W_{SC-coherent}$, the radiation sums from the tunneling probability current and between atoms are treated coherently.

$$\frac{dW_{sc-incoherent}}{d\Omega} = \left(\frac{c}{4\pi}\right) R^2 \int_{-\infty}^{\infty} \left\{ \frac{\sum_i^N \sum_j^M \left(\vec{E}(\vec{R},t)\right)^2}{\sum_i^N \sum_j^M f_j^2(t)} \right\} dt \tag{10}$$

$$\frac{dW_{sc-coherent}}{d\Omega} = \left(\frac{c}{4\pi}\right) R^2 \int_{-\infty}^{\infty} \left\{ \frac{\left(\sum_i^N \sum_j^M \vec{E}(\vec{R},t)\right)^2}{\sum_i^N \left(\sum_j^M f_j(t)\right)^2} \right\} dt \tag{11}$$

With respect to scaling, without normalization the radiated power scales as N for the incoherent W_C and $W_{SC-incoherent}$ cases and as N^2 for the $W_{SC-coherent}$ case.

To understand the difference between coherent and incoherent summation of the radiated field, it is important to make an analogy between the one-photon, two-slit experiment and summation of the radiation across the tunneling ionization current. To accurately describe the one-photon, two-slit experiment, one must have knowledge of the field amplitude on the slits and the relative phase difference for the path from the slits to the detector. The ionization of the electron over space and time creates several paths for the radiation from the electron. At the detector, when the field collapses and the radiated photon is detected, contributions from all paths for the electron probability have to be considered. In fact, as shown in figure 4, the electron probability may extend over 10^{-6} m length scales and introduces a spatial component to the phase of the radiation that could result in interferences. Figure 2.4 shows the radiated electric field for three trajectories from ionization at 1×10^{19} W/cm^2. The figure illustrates that propagation delays can lead to destructive interference of the radiated electric field (when summing coherently) just as the negative and positive fields for the three cases in the figure overlap.

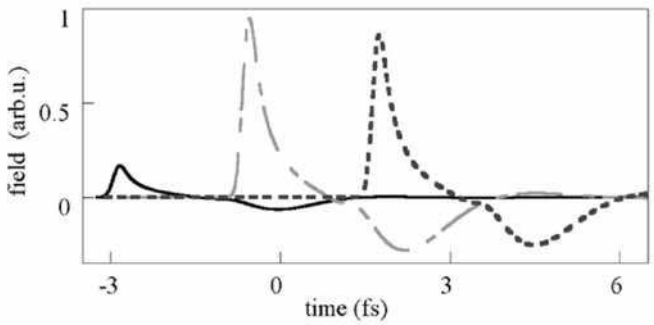

Fig. 6. The E_x field ($\theta = 50°$, $\phi = 0°$) for three trajectories from ionization at $1 \times 10^{19} W/cm^2$.

3. Radiation from ionization in a pulsed, plane wave laser field

3.1 Total energy and power spectrum

Figure 7 shows the total radiated energy from a photoelectron in a one dimensional plane wave laser pulse with the three different treatments of the radiation: classical photoionization and the tunneling probability current summed incoherently and coherently. The radiation yield in the figure is given in units of energy per photoelectron (eV/electron). The results are discussed in terms of three different intensity regimes (Ghebregziabher & Walker, 2007) based on the relative size of the electron quiver motion ($\alpha_0 = a_0/2\pi$, where $a_0 = eE_0/m\omega c$) to the wavelength of the emitted radiation: $\alpha_0 < \lambda/10$ Region I, $\lambda/10 < \alpha_0 < \lambda$ Region II, and $\lambda < \alpha_0$ Region III.

At intensities of $1 \times 10^{17}\ W/cm^2$ ($\alpha_0 = 38\ nm$) and less, highlighted as Region I in the figure, the quiver amplitude is small. In this region, the total radiated energy from a photoelectron, whether classical, semi-classical, coherent, or incoherent, is identical. The quiver amplitude is sufficiently small that interference effects in the radiation are negligible. For laser intensities in the range $1 \times 10^{17}\ W/cm^2$ to $1 \times 10^{19}\ W/cm^2$, Fig. 7 region II) the electron quiver may be up to 300 *nm*. The total radiated energy from a classically ionized electron is still identical to the incoherently summed SC tunneling probability current. However, interference effects in the coherent sum reduce the radiated energy from one-half to one-fifth of the incoherent treatments.

Finally, for laser intensities greater than $1{\times}10^{19}\ W/cm^2$ (Fig. 7 region III), the electron quiver width exceeds the fundamental wavelength. Figure 7 shows for this intensity region the radiated energy from a classically ionized electron and incoherent sum of the tunneling probability current are indistinguishable. Continuing the trend from Region II the coherently summed radiation from the tunneling probability current is fifty times smaller than incoherently summed radiation at an intensity of $1 \times 10^{19}\ W/cm^2$. This is attributed to the 1 micron electron quiver amplitude that results in significant interference effects.

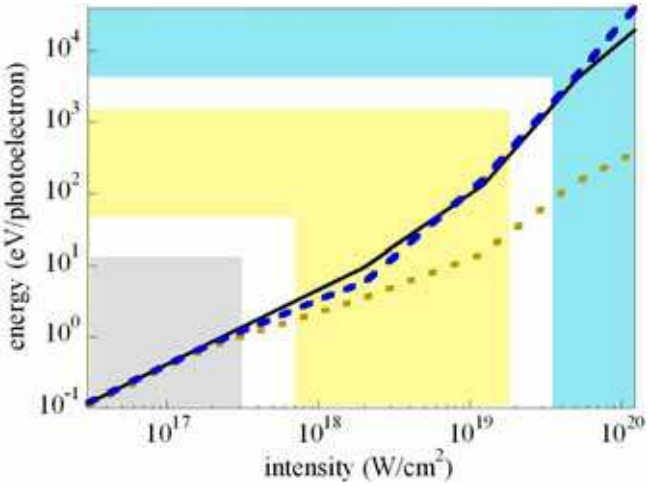

Fig. 7. Radiated energy versus laser intensity from a classically ionized electron (solid, black), incoherently summed tunneling probability current (dashed, blue) and coherently summed tunneling probability current (dotted, dark yellow).

Figure 8 shows the power spectrum of the radiated energy (Fig.7) for intensities (a) 2×10^{17} W/cm^2, (b) 1.2×10^{19} W/cm^2, and (c) 5×10^{19} W/cm^2 with the three models of ionization: MC-ADK, SC-incoherent, and SC-coherent. From the figure, one can see the power spectrum calculated with classical MC-ADK ionization and SC-incoherent model are identical. The radiated power drop at higher intensities seen in Fig. 7 for the coherent sum are manifested as a progressive decrease in the relative high frequency radiation in Fig. 8(a-c). While in Fig. 8 (a) the power spectrum for all cases is nearly identical, in Fig. 8(b,c) the higher frequency radiation is lower by an order of magnitude. This observation corroborates the earlier interpretation of destructive interference for relativistic intensities where the photoelectron excursion is equal to or exceeds the wavelength of the radiation and results in a significant phase shift. The spectral amplitude from coherent averaging over the tunneling probability current is about a factor of 10 less than that from a classically ionized electron. For higher energy photons with $\lambda < \alpha_0$, the spectral amplitude from a classically ionized electron is as large as 35 times that of a coherent average over an ionization probability current. In all cases, up to the maximum intensity of 1×10^{20} W/cm^2 studied, there is no observed difference in the integrated scattered fundamental radiation.

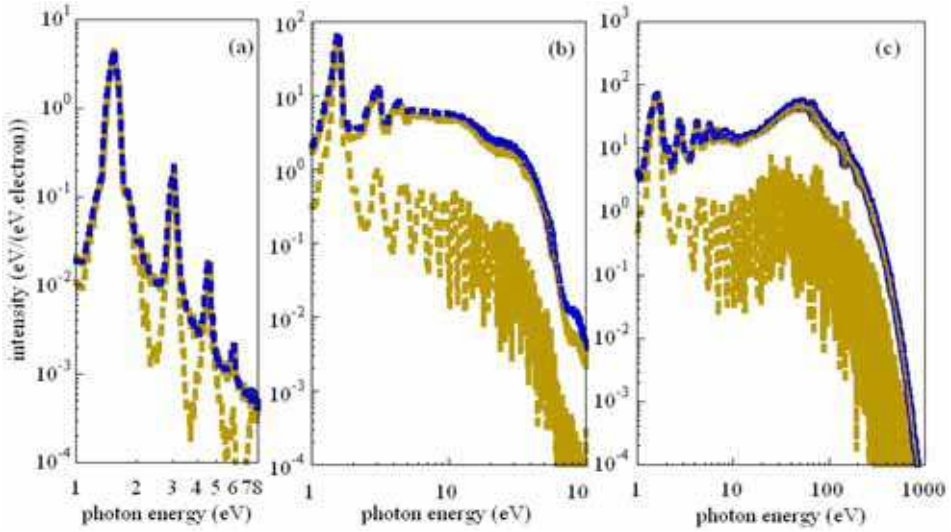

Fig. 8. Total spectral amplitude of the radiated field from atomic ionization at intensities (a) 2×10^{17} W/cm^2, (b) 1.2×10^{19} W/cm^2, and (c) 5×10^{19} W/cm^2 from a classically ionized electron (solid, dark yellow), incoherently summed tunneling probability current (dashed, blue) and coherently summed tunneling probability current (dotted, black).

3.2 Angle resolved radiated energy

The polar angle (θ measured from the $\vec{k}$ vector of the drive laser field) resolved total radiated energy is shown in Fig. 9 from a single classical electron and a tunneling probability current summed coherently in a one-dimensional plane wave laser pulse. (The incoherently summed ionization current result is indiscernible from the classical case). The radiation yield in the figure is given in units of energy per photoelectron per unit angle (eV/photoelectron-degree). At laser intensities from 3×10^{16} W/cm^2 to 2×10^{17} W/cm^2 (Fig.

9(a,b)), the electron motion is non-relativistic with $\gamma = \left(\sqrt{1-\frac{v^2}{c^2}}\right)^{-1}$ = 1.01 to 1.05 and the interaction can be treated in the dipole limit, i.e. the radiated energy shows angular symmetry with maximum radiated energy at a polar angle θ=0° and minimum at θ=90°. As the intensity is increased to $2\times10^{18}\ W/cm^2$ the interaction becomes relativistic ($\gamma \approx 1.5$), which destroys the polar angle dipole radiation pattern symmetry. Furthermore, a clear distinction can be made between a classically ionized electron and coherent radiation treatment from a tunneling probability current. Since the radiation is identical for both methods at θ = 0° (Fig. 9(c-f)) and is increasingly different as one looks in away from k, one can infer the distinction between the two cases has an origin in interference since there is no phase difference in the propagation direction.

As the laser intensity is increased to $1.2\times10^{19}\ W/cm^2$ ($\gamma \approx 4$) the radiation is peaked at θ=60° and resembles more closely the radiation pattern expected for relativistic accelerated charge. For a laser intensity of $5 \times 10^{19}\ W/cm^2$ ($\gamma \approx 12$) the radiation yield from a classically ionized electron is singly peaked at a polar angle θ=30° while radiation from semi-classical ionization treatment with coherent averaging has two peaks located at θ=0° and θ=30°. As mentioned, the radiation yield from the two treatments of ionization at a polar angle θ = 0° is identical; however, as one sweeps to larger polar angles towards the secondary peak at θ = 30° the radiation yield from coherently summed tunneling probability current is drowned by a factor of approximately 50 due to interference. In Fig. 9(f) at $1.2 \times 10^{20}\ W/cm^2$ the electron motion is ultra-relativistic with a peak γ = 30, radiation emitted at θ = 20° and an incredible factor of 100 difference in the peak radiation yield from coherent tunneling ionization probability current compared to that of a classically ionized electron.

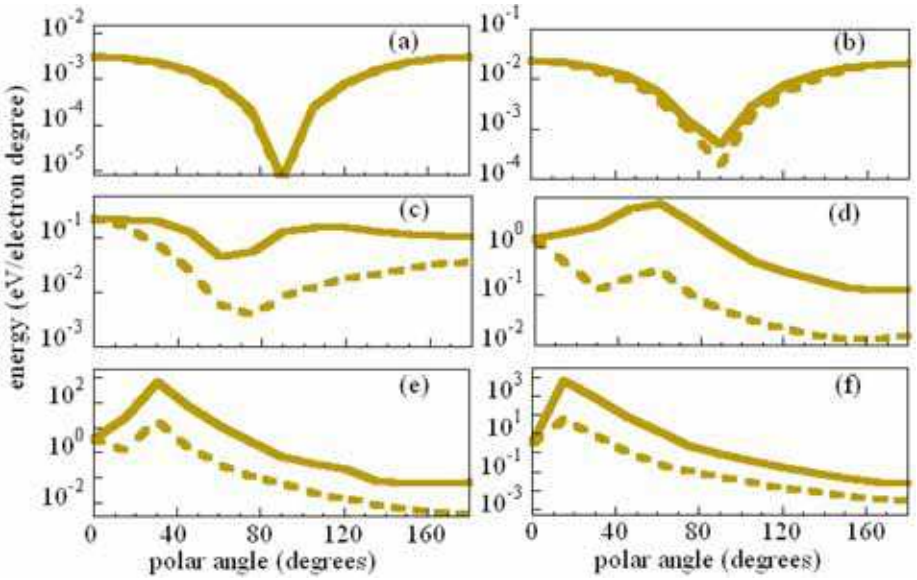

Fig. 9. Angle resolved radiated energy for ionizations in plane wave laser field with peak intensities (a) $3\times10^{16}\ W/cm^2$, (b) $2\times10^{17}\ W/cm^2$, (c) $2\times10^{18}\ W/cm^2$, (d) $1.2\times10^{19}\ W/cm^2$, (e) $5 \times 10^{19}\ W/cm^2$, and (f) $1.2 \times 10^{20}\ W/cm^2$ for a classical photoionization (solid) and coherently summed tunneling probability current (dotted).

4. Radiation from ionization in a pulsed, focused laser field

4.1 Total energy and power spectrum

Until now we have discussed only the results for single ionization event in a 1D plane wave laser pulse. In this section we include radiation in a three-dimensional high intensity laser focus where multiple atoms/ions are distributed randomly and uniformly in the laser focus. The density of atoms is varied to converge on a density independent result while avoiding inter-atomic spacing effects.

Figure 10 shows the total radiated energy from classical MC-ADK ionization and SC-coherent ionization in a three dimensional laser pulse. The radiation yield is normalized in the figure to the total amount of photoionization with units of energy per photoelectron (eV/electron). Figure 10 shows at intensities of $1\times10^{17}\,W/cm^2$ and less, highlighted as Region I in the figure, there is a slightly more of a difference between W_c and $W_{sc-coherent}$ compared to Fig. 11(a). Overall though, the results are consistent with the 1D plane wave results. Any difference from the plane wave case is expected to be rooted in the increased drift energy of the electron from the acceleration of the photoelectron out of the focus. For laser intensities in the range ($2\times10^{17}\,W/cm^2$ to $5\times10^{19}\,W/cm^2$, Figs. 10,11), the results in the focal geometry case are qualitatively identical to those for the one-dimensional analysis, i.e. a reduction in the high frequency radiation due to interference in the extended tunneling ionization probability current compared to the „perfect" coherence of a point, classical electron.

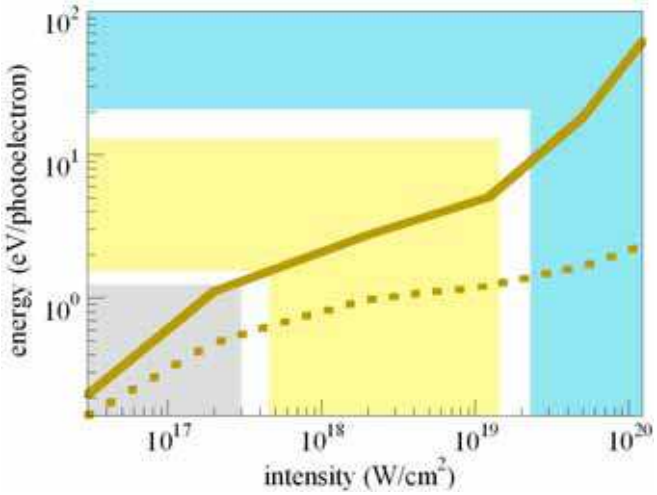

Fig. 10. Radiated energy versus laser intensity from classical photoionization (solid), and coherently summed tunneling probability current (dotted). Three regions (see text) are highlighted in the figure.

Closer examination of Fig. 7 and Fig. 8, however, reveals a significant difference between the idealized 1D case and the 3D focal geometry used in experiments. In Region II and III, the quantitative yields do not agree. Beginning at about $1\times10^{18}\,W/cm^2$ the yields diverge. While in the one-dimensional case the radiated energy for the incoherent (coherent) mechanism increases as $I^{1.5}$ ($I^{0.8}$) in Region II to $I^{1.8}$ ($I^{1.1}$) for Region III, for the 3D case the intensity dependence in Region II is only $I^{0.34}$ ($I^{0.11}$) and $I^{1.36}$ ($I^{0.4}$) in Region III. By a few times 1×10^{19}

W/cm^2, all radiation yields are 10 times lower for the focal geometry case than the respective yields in the plane wave case. This difference in the intensity dependence is due to electron-electron interferences between atoms ionized at different locations in a laser focus. Comparing the results at the peak intensity of $1 \times 10^{20}\ W/cm^2$ the coherent superposition of the radiation across the focal geometry has a larger effect than any difference in the way the ionization is treated; the degree of the coherence of the radiation across the focus can affect the radiation yield to a greater extent than the incoherent or coherent treatment of the radiation during the ionization process. Figure 6 is a plot of the power spectrum for the radiated harmonics at three different focal intensities. As one compares Fig. 8 to Fig. 11(c) the absolute difference in the radiation is 100 times for first few harmonics and 1000 times for the radiation near $100eV$.

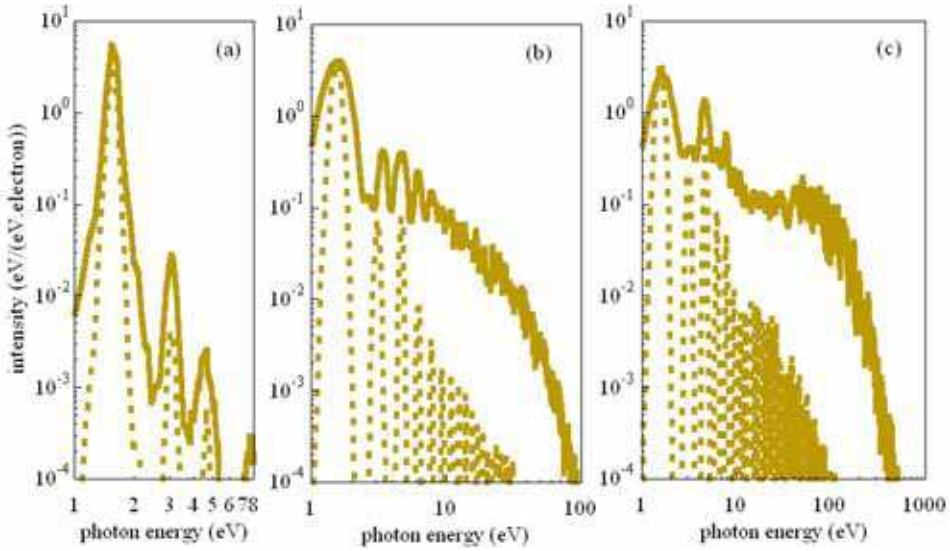

Fig. 11. Total spectral amplitude of the radiated field from atomic ionization at intensities (a) $2 \times 10^{17} W/cm^2$ (b) $1.2 \times 10^{19} W/cm^2$ and (c) $5 \times 10^{19} W/cm^2$ from classical photoionization (solid) and coherently summed tunneling probability current (dotted).

4.2 Angle resolved radiated energy

The angle and energy resolved radiation yields are presented in Fig. 12 for the focal geometry case. The plots are comparable to Fig. 8 but offer the additional derivative of the yields as a function of frequency. The radiation from classically ionized photoelectrons (essentially synonymous with the incoherently summed tunneling probability current) are shown in Fig. 12 (a, c, e, g, i) and the coherent tunneling probability current results in Fig. 12 (b, d, f, h, j). The logarithmic scale used in the plot is normalized to the peak radiation yield from classically ionized electrons in the respective laser field intensity.

An inspection of Fig. 12 reveals as one progresses beyond the dipole response (Fig. 12(a,b)) to ultrahigh fields coherently interfering radiation consistently occurs at larger angles in θ compared to incoherently summed or classical ionization. Furthermore the cutoff, or high frequency radiation, is always lower for coherently summed radiation by factors of 3 to 4

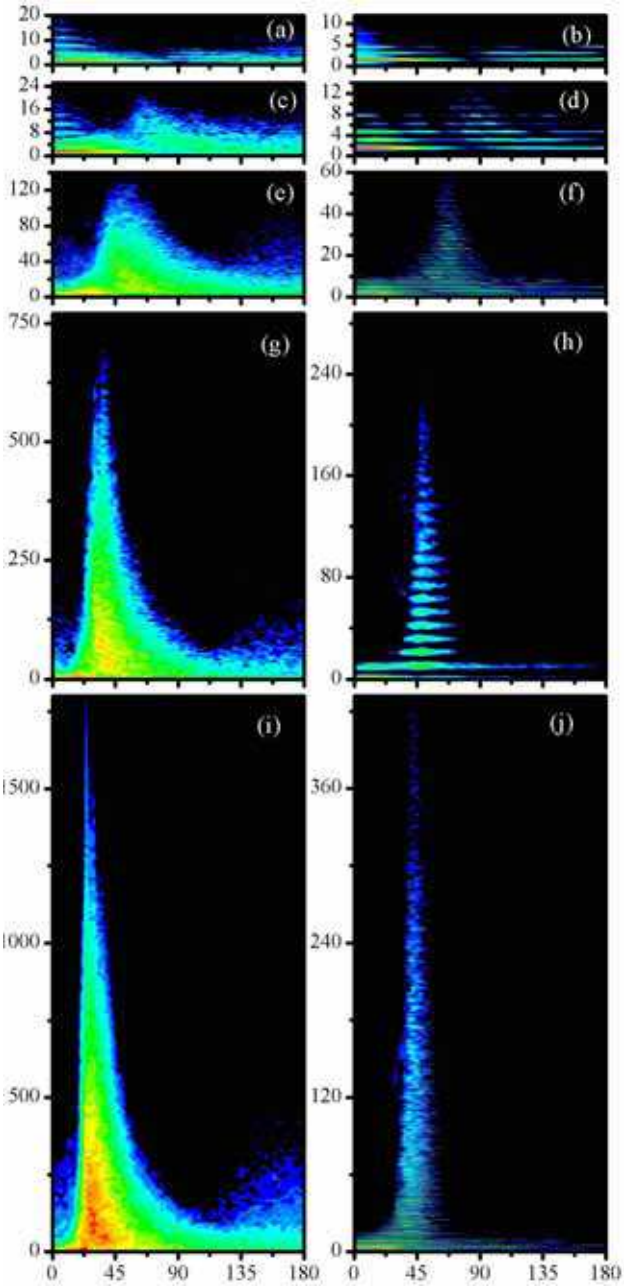

Fig. 12. Angle-and frequency resolved total radiation yield for (a,b) $2 \times 10^{17} W/cm^2$, (c,d) $2 \times 10^{18} W/cm^2$, (e,f) $1.2 \times 10^{19} W/cm^2$, (g,h) $5 \times 10^{19} W/cm^2$, and (i,j) $1.2 \times 10^{20} W/cm^2$ for classical (a,c,e,g,i) and coherently summed tunneling probability current (b,d,f,h,j).

when the intensities are between $1\times10^{19} W/cm^2$ and $1\times10^{20} W/cm^2$. This poses some difficulty for experiments since the difference between coherent and incoherent radiation is similar to the difference one would expect by a simple change in intensity. The possibility for confusion in this case of alternate causality can be seen by comparing, for example, Fig. 12(h) for coherent radiation at $5 \times 10^{19} W/cm^2$ with Fig 12(e) for incoherent radiation at $1.2 \times 10^{19} W/cm^2$. Similar comparisons can be made for Fig. 12(j) to Fig. 12(g). This observation combined with the N^2 effect of the focal geometry, the clearest identification of coherence from radiation in ultrastrong fields may come from the intensity dependence of the radiated power.

The radiation yield from the highest intensities studied involve photoionization at a peak intensity of $1.2 \times 10^{20} W/cm^2$. The radiation is peaked at a polar angle ($\theta \sim 34°$) for classically ionized electrons and ($\theta \sim 45°$) semi-classical ionization case with a cutoff photon energy for classically ionized electrons extending out to ($h\nu \sim 1.75 KeV$) while for semi-classical ionization it extends out to ($h\nu \sim 420 eV$).

5. Effect of focal geometry on radiation

In this section the primary effect of the 3-dimensional nature of the laser focus is quantified by comparing emitted radiation in a plane wave approximation and focused geometry cases calculated with the MC-ADK radiation model discussed above.

5.1 Laser intensity dependence of total radiated energy and spectrum

Figure 13(a) shows the total radiated energy as calculated using plane wave approximation of the laser field (dotted) and the three-dimensional laser field (solid). The radiation yield is normalized in the figure to the total amount of photoionization with units of energy per photoelectron (eV/electron). Fig. 13(a) shows at intensities of $1\times10^{17}\ W/cm^2$ and less, highlighted as region I in the figure, there is very little difference between radiation using a plane wave or focus geometry. This is associated with the small electron quiver amplitude ($\alpha_0 = a_0\lambda/2\pi$, where $a_0 = eE_0/m$) at $1 \times 10^{17} W/cm^2$, which extends out to 38 nm or less than a few percent of the focal waist radius (half-width at half-maximum $r_0 = \frac{2\sqrt{\ln 2} f/\#\lambda}{\pi}$). The limit where $\alpha_0 \leq r_0/10$, which we call region I, is also shown in Fig. 13(b) where the ratio of the electron excursion α_0 to the half width half maximum of the laser intensity at the focus r_0 is plotted as a function of intensity in the focus. In region I neglecting the spatial variation of the laser focus and adopting a one-dimensional laser field for radiation calculations is corroborated by the spectral amplitudes of the radiated field shown in Fig. 14(a). Out to the cutoff in the radiation at about 10 eV there is no difference between the spectra for photoionization in a plane wave or laser focus.

For laser intensities in the range ($2 \times 10^{17}\ W/cm^2$ to $1.5 \times 10^{19}\ W/cm^2$,, Fig. 13 region II) the electron quiver width may be up to 300 nm, which is in the range of 0.1 to 0.5 times the beam waist radius of the laser focus. Since the electron travels non-negligible distances compared to the beam waist radius of the laser focus, it effectively experiences an average field that is lower than the peak field. In region II, adopting the plane wave approximation of the laser field overestimates the total radiated energy compared to the 3D focal geometry. Despite this drop in the total radiated energy from the first few harmonics, the extra velocity from surfing begins to play a role and the result is the higher photon energy persists in region II.

As one can in Fig. 14(b), for $h\nu > 7\ eV$, the radiation may be enhanced in the 3D focus case due to the acceleration of the photoelectron as it exits the focus. In addition, the laser focus and small α_0 confine the laser radiation to less than a cubic micron leading to a more coherent radiation than the plane wave approximation, where the sources of radiation span infinite space.

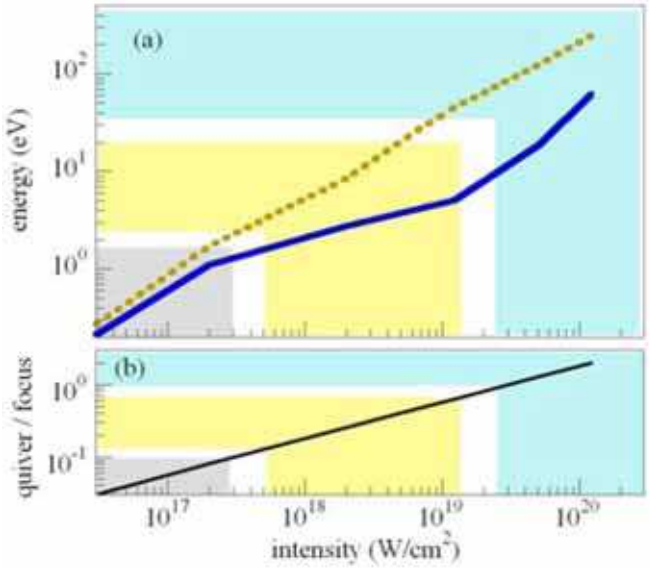

Fig. 13. Radiated energy versus laser intensity (a) with plane wave approximation (dotted, yellow-orange), and non-paraxial approximation (solid, blue). Three regions (see text) are highlighted in the figure.

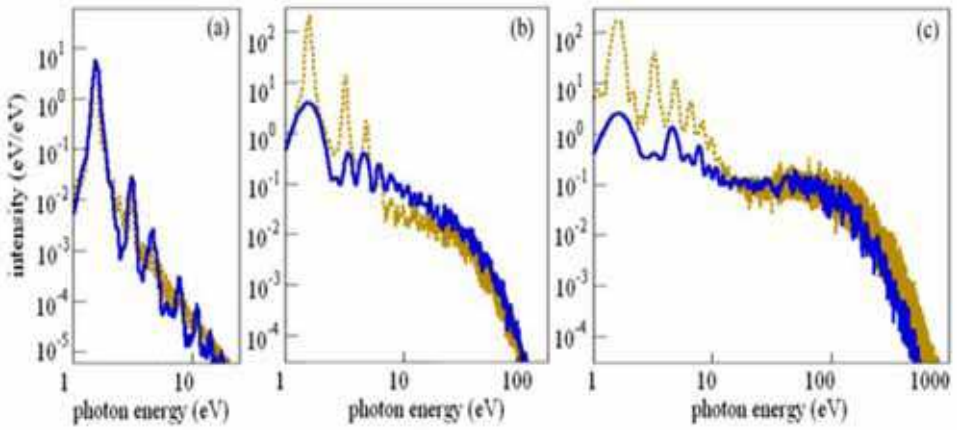

Fig. 14. Total spectral amplitude of the radiated field from atomic ionization at intensities $2\times10^{17}\ W/cm^2$ (a), $1.22\times10^{19}\ W/cm^2$(b), and $5\times10^{19}\ W/cm^2$ (c) calculated using the plane wave approximation (dotted, yellow-orange), non-paraxial approximation (solid-blue).

Figures 14 shows the spectral amplitude of the radiated field for laser light intensities of 2 × $10^{17}\ W/cm^2$ (a), 1.22 × $10^{19}\ W/cm^2$ (b) and 5 × $10^{19}\ W/cm^2$ (c) calculated using the plane wave (dotted) and focal geometry (solid). The marked reduction in the intensity of the first three harmonics can be seen in Fig. 14(b) and is responsible for the lower radiated power in Fig. 13. One can also see in Fig. 14(b) the aforementioned increase in the highest photon energy radiation ($h\nu > 7\ eV$).

For laser intensities greater than 1.22 × $10^{19}\ W/cm^2$ (Fig. 13 region III), the electron quiver width approaches 1 μm, which is larger than the beam waist radius of the laser focus. In region III, as with region II the photoelectron experiences an effectively smaller field compared to a plane wave at the same intensity. The effect is greater however with a reduced acceleration of the electron for its entire trajectory. This also means the electron will gain an extra boost of speed as it surfs out of the laser focus as shown in Fig. 5(b); but, the extra boost is not able to overcome the reduction in field from the prompt exit of the electron. Compared to region I and II, region III and radiation from ultrastrong fields comes from the largest spatial volume connected with the large α_0. Overall the total radiation from the focus geometry is significantly less than in the plane wave case.

6. Sequential ionization charge state contribution to the radiation yield

In this final section we discuss the expected results for radiation observed from a charge state distribution rather than the single, highest intensity charge state previously discussed. Here we include the impact of radiation as the intensity increases in the pulse and across the intensity distribution of the focus from the charge states generated when the laser ionizes neutral atoms up to the highest charge state. The total radiation yield is normalized by the total number of photoelectrons generated from all charge states in the respective laser foci.

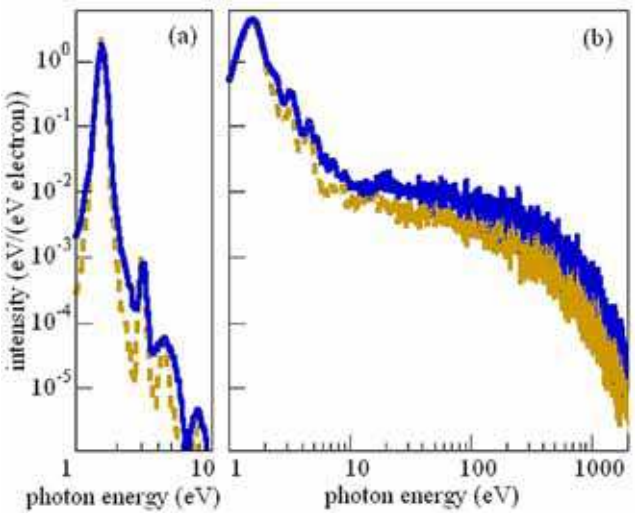

Fig. 15. Total radiated spectral intensity with full focal volume averaged (dotted, orangeyellow) and final charge state only (solid, blue) calculated with non-paraxial approximation at laser intensities of 2 × $10^{17}\ W/cm^2$ (a) and 1.22 ×$10^{20}\ W/cm^2$(b).

The numerical values of the peak radiation from ionizing neutral atoms to highest charge state and ionizing highest charge state only, are the same. In both cases, the radiation yield is the highest for the first few lowest harmonics. The small differences, seen for example in Fig. 15(a, b), are the natural result of averaging over multiple charge states for species with varying ionization potentials. In Fig. 15(a, b) this results in narrower more resolved peaks for the harmonics. Also, due to the increase in photoelectrons from species ionized at low intensities the first harmonic radiation is enhanced, which appears as a decrease in the 3 eV to 2000 eV portion of the spectrum due to the normalization choice on the highest intensity/first harmonic.

The angle and energy resolved radiation yields from sequentially ionized neutrals (Ar and Na atoms) to their possible highest charges states Ar^{16+}, Na^{10+} and Na^{11+} in laser intensities $1.22 \times 10^{19}\ W/cm^2$, $5 \times 10^{19}\ W/cm^2$, and $1.22 \times 10^{20}\ W/cm^2$, respectively, are shown in Fig. 16 (a, c, e). Also shown in the figure is the radiation contribution from the highest charge state only (Fig. 16 (b, d, e)). The peak radiation from photoionization of these atoms/ions in a laser focus occurs at the fundamental frequency.

The logarithmic scale used in the plot is normalized to the peak radiation yield. The contribution to the radiation yield from the lower charge states is in the lowest harmonics since photoelectrons from low charge states are ionized in the beginning of the pulse, and leave the laser focus without experiencing the peak of the laser field, or are in the spatial wings of the pulse where the peak intensity is lower. To make valid comparison of the full ionization case, a logarithmic scale plot is shown similar to Fig. 12 for the polar angle dependence. Comparison of the results (Fig. 16(a, b), 16(c, d), 16(e, f)) shows focal averaging doesn't have noticeable effect on cutoff energies, polar angle peaking and angular divergence of the radiation yield.

7. Conclusion

These results on the radiation from ultrahigh field ionized atoms have characterized the role of coherence on the yield from the dipole response up to the currently known limit of tunneling ionization at $1 \times 10^{20}\ W/cm^2$. The results reported here expand our understanding in ultrastrong fields to include (1) a more detailed classical Monte Carlo ADK ionization mechanism for the photoionization, (2) the 3D focal geometry common to high field experiments, (3) electron wave packet spreading and coherence, and (4) the results when including radiation from the sequential ionization lower charge states in route to the ionization of the final charge state at the peak field. Our results are interpreted with the ratio of the photoelectron excursion to the laser focus and wavelength.

We find a classical view of ionization results in the same yield as a tunneling ionization probability current treatment when the radiation sum across the current is done incoherently. In the case that one assumes perfect coherence of the radiation across the tunneling current, the observed radiation decreases when the excursion of the photoelectron is comparable to the wavelength of the emitted radiation due to interference in the far field. When comparing the plane wave case to the focal geometry, the coherence of the radiation across the micrometer spatial extend of the focus has a larger affect on the observed yields the degree of coherence within the tunneling ionization current and interference from the photoelectron excursion for a single photoionization event. Additional difficulties may be faced by experimental studies because changes in the coherence and changes in the intensity can have a similar effect on the observed radiation.

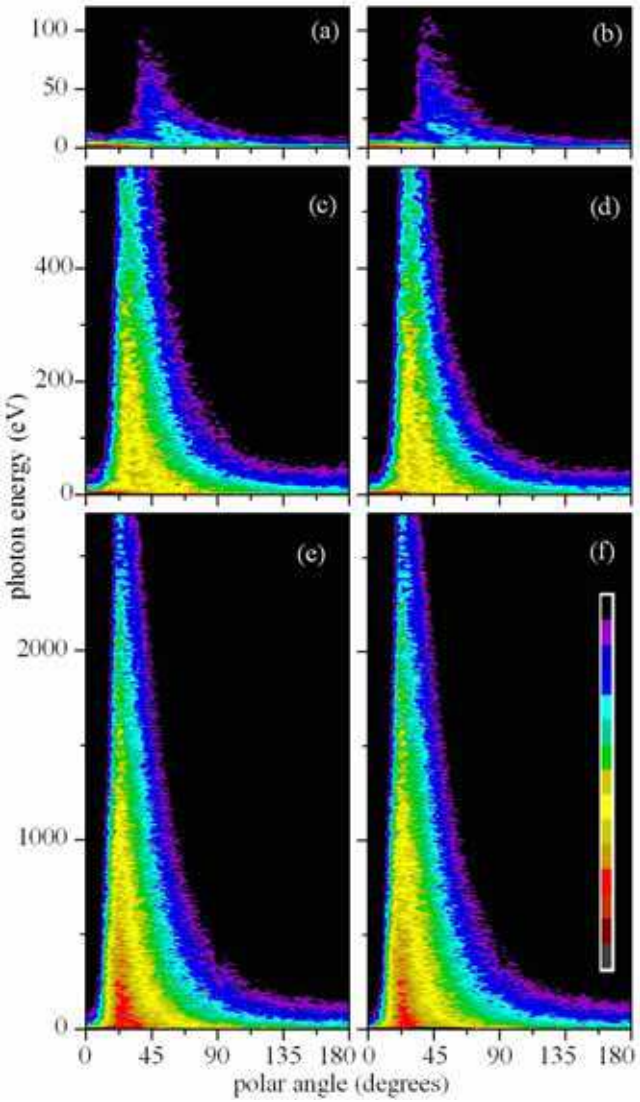

Fig. 16. Angle-and frequency resolved total radiation yield for intensities $1.22 \times 10^{19}\, W/cm^2$ (a, b), $5 \times 10^{19}\, W/cm^2$ (c, d), and $1.22 \times 10^{20}\, W/cm^2$ (e, f) from full sequential ionization of Ne-Ne^{+7} (a), Na-Na^{+10} (c), Na-Na^{+11} (e) and the highest charge state only (b, d, f). The magnitude scale inset in (f) ranges from unity to exp(-14) in steps of exp(-1) for all plots.

In fields where the excursion is less than the focus waist (Fig. 13, region I) the radiation from a focus and plane wave are indistinguishable. In fields as high as $1 \times 10^{19}\, W/cm^2$ (Fig. 13, region II), where the single cycle laser driven excursion of the photoelectron is comparable to the laser focus, the radiated power in a focal geometry drops by a factor between 2 and 10

for the lowest harmonics compared to a plane wave; but, the expected radiation near cutoff is very comparable for the two cases. In the highest fields (Fig. 13, region III), the photoelectron is unable to experience the peak laser intensity when radiation is probable and the observed cutoff radiation and angle are reduced in the focus geometry case to reflect the overall lower effective intensity. For a given peak field, the focal geometry is analogous to results one may expect at half the peak intensity for a plane wave. The results are not significantly changed if one considers only the radiation from photoelectrons near the peak of the field or when radiation from sequential ionization of the preceding charge states of the atom are included.

This material is based upon work supported by the Army Research Office under Award No. W911NF-09-1-0390 and the National Science Foundation under Award No. 0757953.

8. References

Albert, O., Wang, H., Liu, D., Chang, Z. & Mourou, G. (2000). Generation of relativistic intensity pulses at a kilohertz repetition rate, *Optics Letters* 25: 1125.

Ammosov, M. V., Delone, N. B. & Krainov, V. P. (1986). Tunnel ionization of complex atoms and of atomic ions in an alternating electromagnetic field, *Sov.Phys.JETP* 64: 1191.

Barton, J. & Alexander, D. (1989). Fifth-order corrected electromagnetic field components for a fundamental Gaussian beam, *Journal of Applied Physics* 66: 2800–2802.

Chen, S.-Y., Maksimchuk, A. & Umstadter, D. (1998). Experimental observation of relativistic nonlinear Thomson scattering, *Nature* 396: 653.

Chowdhury, E. A., Ghebregziabiher, I. & Walker, B. C. (2005). Larmor radiation from the ultra-intense field ionization of atoms, *Journal of Physics B Atomic Molecular Physics* 38: 517–524.

Clark, E. L., Krushelnick, K., Davies, J. R., M. Zepf, M. T., Beg, F. N., Machacek, A., Norreys, P. A., Santala, M. I. K., Watts, I. & Dangor, A. E. (2000). Measurements of energetic proton transport through magnetized plasma from intense laser interactions with solids, *Phys. Rev. Lett.* 84: 670.

Corkum, P. (1993). Plasma perspective on strong field multiphoton ionization, *Phys.Rev.Lett.* 71: 1994–1997.

Davis, L.W. (1979). Theory of electromagnetic beams, *Physical Review A* 19(3): 1177.

Esarey, E., Ride, S. K. & Sprangle, P. (1993). Nonlinear Thomson scattering of intense laser pulses from beams and plasmas, *Physical Review E* 48(4): 3003.

Ghebregziabher, I. & Walker, B. C. (2007). Effect of focal geometry on radiation from atomic ionization in an ultrastrong and ultrafast laser field, *Phys.Rev.A* 76(2): 023415.

Ghebregziabher, I. & Walker, B. C. (2008). Impact of coherence in radiation from ultrahigh-field atomic ionization, *Phys. Rev. A* 77: 023417.

Hu, S. X. & Starace, A. F. (2002). GeV Electrons from Ultraintense Laser Interaction with Highly Charged Ions, *Physical Review Letters* 88(24): 245003.

Jackson, J. (1975). *Classical Electrodynamics*, second edn, John wiley and Sons, New York.

Keitel, C. H. & Knight, P. L. (1995). Monte Carlo classical simulations of ionization and harmonic generation in the relativistic domain, *Phys.Rev.A* 51: 1420–1430.

Kneip, S., Nagel, S. R., Martins, S. F., Mangles, S. P. D., Bellei, C., Chekhlov, O., Clarke, R. J., Delerue, N., Divall, E. J., Doucas, G., Ertel, K., Fiuza, F., Fonseca, R., Foster, P., Hawkes, S. J., Hooker, C. J., Krushelnick, K., Mori, W. B., Palmer, C. A. J., Phuoc, K. T., Rajeev, P. P., Schreiber, J., Streeter, M. J. V., Urner, D., Vieira, J., Silva, L. O. & Najmudin, Z. (2009). Near-gev acceleration of electrons by a nonlinear plasma wave driven by a self-guided laser pulse, *Phys. Rev. Lett.* 103(13): 035002.

Lau, Y., He, F., Umstadter, D. & Kowalczyk, R. (2003). Nonlinear thomson scattering: A tutorial, *Physics of Plasmas* 10: 2155–2162.

Lee, K., Kim, B. H. & Kim, D. (2005). Coherent radiation of relativistic nonlinear Thomson scattering, *Physics of Plasmas* 12: 043107.

Leemans,W. P., Nagler, B., Gonsalves, A. J., Tth, C., Nakamura, K., Geddes, C. G. R., Esarey, E., Schroeder, C. B. & Hooker, S. M. (2006). Gev electron beams from a centimetre-scale accelerator, *Nature Physics.* 2: 696.

Mocken, G. & Keitel, C. (2005). Radiation spectra of laser-driven quantum relativistic electrons, *Computer Physics Communications* 166: 171–190.

Palaniyappan, S., DiChiara, A., Ghebregziabher, I., Huskins, E. L., Pajerowski, A. F. D. & Walker, B. C. (2006). Multielectron ultrastrong laser field ionization of Ar^{n+}, Kr^{m+} and Xe^{l+} ($n \leq 9, m \leq 9, l \leq 12$) at intensities from 1×10^{15} Wcm^{-2} to 1×10^{18} Wcm^{-2}, *Journal of Physics B Atomic Molecular Physics* 39: 357.

Peatross, J., Muller, C., Hatsagortsyan, K. Z. & Keitel1, C. H. (2008). Photoemission of a singleelectron wave packet in a strong laser field, *Phys. Rev. Lett.* 100: 153601.

Perelomov, A., Popov, V. & Terentev, M. (1966). Ionization of atoms in an alternating electric field, *Sov.Phys.JETP* 64: 1191.

Phuoc, K. T., Rousse, A., Pittman, M., Rousseau, J., Malka, V., Fritzler, S., Umstadter, D. & Hulin, D. (2003). X-Ray Radiation from Nonlinear Thomson Scattering of an Intense Femtosecond Laser on Relativistic Electrons in a Helium Plasma, *Physical Review Letters* 91(19): 195001.

Popov, V. S. (2004). Tunnel and multiphoton ionization of atoms and ions in a strong laser field (keldysh theory), *Physics-Uspekhi* 47(9): 855–885.

Rousse, A., Phuoc, K. T., Shah, R., Pukhov, A., Lefebvre, E., Malka, V., Kiselev, S., Burgy, F., Rousseau, J.-P., Umstadter, D. & Hulin, D. (2004). Production of a kev x-ray beam from synchrotron radiation in relativistic laser-plasma interaction, *Phys. Rev. Lett.* 93(13): 135005.

Schoenlein, R.W., Leemans,W. P., Chin, A. H., Volfbeyn, P., Glover, T. E., Balling, P., Zolotorev, M., Kim, K. J., Chattopadhyay, S. & Shank, C. V. (1996). Femtosecond x-ray pulses at 0.4 å generated by 90° thomson scattering: A tool for probing the structural dynamics of materials, *Science* 274(5285): 236.

Schwoerer, H., Liesfeld, B., Schlenvoigt, H. P., Amthor, K. & Sauerbrey, R. (2006). Thomsonbackscattered x rays from laser-accelerated electrons, *Phys. Rev. Lett.* 96: 014802.

Snavely, R. A., Key, M. H., Hatchett, S. P., Cowan, T. E., Roth, M., Phillips, T., Stoyer, M. A., Henry, E. A., Sangster, T. C., Singh, M. S., Wilks, S. C., MacKinnon, A., Offenberger, A., Pennington, D., Yasuike, K., Langdon, A. B., Lasinski, B. F., Johnson, J., Perry,

M. D. & Campbell, E. M. (2000). Intense high-energy proton beams from petawattlaser irradiation of solids, *Phys. Rev. Lett.* 85: 2945.

Tate, J., Auguste, T., Muller, H., Salières, P., Agostini, P. & Dimauro, L. (2007). Scaling of Wave-Packet Dynamics in an Intense Midinfrared Field, *Physical Review Letters* 98(1): 013901.

Ueshima, Y., Kishimoto, Y., Sasaki, A. & Tajima, T. (1999). Laser Larmor X-ray radiation from low-Z matter, *Laser and Particle Beams* 17: 45–58.

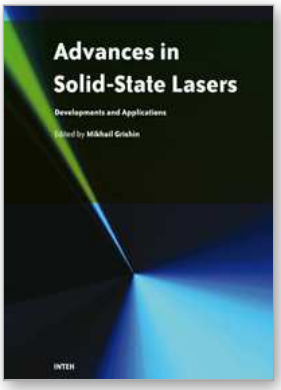

Advances in Solid State Lasers Development and Applications

Edited by Mikhail Grishin

ISBN 978-953-7619-80-0
Hard cover, 630 pages
Publisher InTech
Published online 01, February, 2010
Published in print edition February, 2010

Invention of the solid-state laser has initiated the beginning of the laser era. Performance of solid-state lasers improved amazingly during five decades. Nowadays, solid-state lasers remain one of the most rapidly developing branches of laser science and become an increasingly important tool for modern technology. This book represents a selection of chapters exhibiting various investigation directions in the field of solid-state lasers and the cutting edge of related applications. The materials are contributed by leading researchers and each chapter represents a comprehensive study reflecting advances in modern laser physics. Considered topics are intended to meet the needs of both specialists in laser system design and those who use laser techniques in fundamental science and applied research. This book is the result of efforts of experts from different countries. I would like to acknowledge the authors for their contribution to the book. I also wish to acknowledge Vedran Kordic for indispensable technical assistance in the book preparation and publishing.

How to reference

In order to correctly reference this scholarly work, feel free to copy and paste the following:

Isaac Ghebregziabher and Barry Walker (2010). Radiation Dynamics from the Ultra-Intense Field Ionization of Atoms, Advances in Solid State Lasers Development and Applications, Mikhail Grishin (Ed.), ISBN: 978-953-7619-80-0, InTech, Available from: http://www.intechopen.com/books/advances-in-solid-state-lasers-development-and-applications/radiation-dynamics-from-the-ultra-intense-field-ionization-of-atoms

INTECH
open science | open minds

InTech Europe
University Campus STeP Ri
Slavka Krautzeka 83/A
51000 Rijeka, Croatia
Phone: +385 (51) 770 447
Fax: +385 (51) 686 166
www.intechopen.com

InTech China
Unit 405, Office Block, Hotel Equatorial Shanghai
No.65, Yan An Road (West), Shanghai, 200040, China
中国上海市延安西路65号上海国际贵都大饭店办公楼405单元
Phone: +86-21-62489820
Fax: +86-21-62489821